



# Flexible biodegradable citrate-based polymeric step-index optical fiber



Dingying Shan <sup>a,1</sup>, Chenji Zhang <sup>b,1</sup>, Surge Kalaba <sup>a</sup>, Nikhil Mehta <sup>b</sup>, Gloria B. Kim <sup>a</sup>, Zhiwen Liu <sup>b,\*</sup>, Jian Yang <sup>a,\*</sup>

<sup>a</sup> Department of Biomedical Engineering, Materials Research Institute, The Huck Institutes of the Life Sciences, The Pennsylvania State University, University Park, PA, 16802, USA

<sup>b</sup> Department of Electrical Engineering, Materials Research Institute, The Pennsylvania State University, University Park, PA, 16802, USA

## ARTICLE INFO

### Article history:

Received 7 June 2017

Received in revised form

28 July 2017

Accepted 3 August 2017

Available online 4 August 2017

### Keywords:

Biodegradable

Implantable

Elastomers

Optical fibers

Imaging

## ABSTRACT

Implanting fiber optical waveguides into tissue or organs for light delivery and collection is among the most effective ways to overcome the issue of tissue turbidity, a long-standing obstacle for biomedical optical technologies. Here, we report a citrate-based material platform with engineerable opto-mechano-biological properties and demonstrate a new type of biodegradable, biocompatible, and low-loss step-index optical fiber for organ-scale light delivery and collection. By leveraging the rich designability and processibility of citrate-based biodegradable polymers, two exemplary biodegradable elastomers with a fine refractive index difference and yet matched mechanical properties and biodegradation profiles were developed. Furthermore, we developed a two-step fabrication method to fabricate flexible and low-loss (0.4 db/cm) optical fibers, and performed systematic characterizations to study optical, spectroscopic, mechanical, and biodegradable properties. In addition, we demonstrated the proof of concept of image transmission through the citrate-based polymeric optical fibers and conducted *in vivo* deep tissue light delivery and fluorescence sensing in a Sprague–Dawley (SD) rat, laying the groundwork for realizing future implantable devices for long-term implantation where deep-tissue light delivery, sensing and imaging are desired, such as cell, tissue, and scaffold imaging in regenerative medicine and *in vivo* optogenetic stimulation.

© 2017 Elsevier Ltd. All rights reserved.

## 1. Introduction

A long-standing hurdle, which has greatly plagued biomedical optical technologies, is the turbidity of biological tissues. Due to significant scattering and absorption loss, light cannot be efficaciously delivered to or collected from target regions within deep tissue, significantly hindering our capability to monitor post-surgical healing of tissues or organs, perform highly targeted light-based therapy, or optogenetic stimulation, to name but a few examples. Implanting fiber optical waveguide in tissues or organs for light delivery or collection is one of the most effective methods for alleviating this problem [1]. However, traditional silica fibers are not only non-degradable, but also fragile and brittle in nature, thus presenting a significant limitation as an implantable device [2].

Waveguides made from single traditional materials, such as poly(ethylene glycol) (PEG) [3], silk [4], agarose gel [5], and poly(L-lactic acid) (PLA) [6] have also been reported. However, due to the lack of an intrinsic cladding layer, single material waveguides tend to have high loss, resulting from significant interaction of the guided optical wave with surrounding medium (such as tissues *in vivo*). To address this issue, a biocompatible step-index fiber optical waveguide consisting of a PEG core and an alginate hydrogel cladding was developed for organ-scale light delivery and collection [7]. Later, fibers having step-index structure but made of alginate-polyacrylamide hydrogel [8] and silk [9] were also demonstrated. Despite the progress, hitherto the underlying materials either suffer from non-degradability or have limited processability and designability. In general, a fundamental challenge of the field is the lack of a suitable material platform that can simultaneously meet the diversified requirements on optical (tailored refractive indices for both the core and the cladding, low optical loss), mechanical (tunable mechanical flexibility for tissue

\* Corresponding authors.

E-mail addresses: [zliu@psu.edu](mailto:zliu@psu.edu) (Z. Liu), [jxy30@psu.edu](mailto:jxy30@psu.edu) (J. Yang).

<sup>1</sup> Both authors contributed equally and are listed by alphabetic order.

compliance), and biological (biocompatibility and programmable biodegradability) functionalities.

Here we present a biocompatible and biodegradable step-index optical fiber that is fabricated from citrate-based polymeric elastomers. Citric acid, a Krebs cycle intermediate is the key component used in the citrate methodology, through which various cross-linkable elastomeric polymers can be synthesized by reacting the multifunctional citric acid with different diols and/or amino acids via a facile polycondensation reaction [10–13]. Unlike natural materials (e.g., silk) or traditional synthetic polymers (e.g., poly lactic-co-glycolic acid (PLGA)) that usually have limited tunability for key optical, mechanical, and/or degradation properties, the family of citrate-based biodegradable elastomers possesses tunable mechanical strengths (from tens of Pascal to mega Pascal), programmable degradation rates (from a few days to over a year), reactive nature between citrate-based polymers, multifunctionalities (e.g., adhesive, fluorescent) [14], and as shown in this work, ultrafine tuning of refractive index ( $\sim 10^{-3}$ ) (Fig. 1c). Citrate-based elastomers have been used as implant materials for diverse applications such as soft tissue engineering (blood vessel, nerve, and skin) [15–17], bone tissue engineering [18–21], wound healing and bioadhesives [22–26], theranostic nanoparticles for cancer imaging and drug delivery [12,27–33], and biosensing [34]. Therefore, citrate-based elastomers serve as an ideal material platform for the development of fully biodegradable and seamlessly integrated step-index optical fibers for *in vivo* applications.

## 2. Methods

### 2.1. Synthesis of POC and POMC pre-polymers

To prepare POC pre-polymer, citric acid (CA) and 1,8-octanediol (OD) with a molar ratio of 1:1 were added to a round-bottom flask, and the mixture was melted within 20 min by stirring the contents in the flask at 160 °C. Once the constituents melted, the temperature was changed to 140 °C and the reaction was allowed to progress for an additional 1.5 h to produce the POC pre-polymer. For the preparation of POMC pre-polymer, CA, maleic anhydride (MAN), and OD, with a feeding molar ratio of 0.4: 0.6: 1.0, were mixed and reacted based on the same procedure as the POC pre-polymer synthesis.

### 2.2. Fabrication of step-index fibers

A two-step fabrication method was developed to achieve the core-cladding bilayer structure. The schematic diagram of the fabrication process is shown in Fig. 2a. In Step 1, the cladding layer was prepared by using a surface-polished stainless steel wire with a diameter of 500  $\mu\text{m}$  as the mold. The melted POC pre-polymer liquid was applied to the surface of the metal wire and thermally crosslinked at 70 °C for 4 days. In order to detach the POC cladding tube from the wire, the polymer-coated wire was immersed in 30% ethanol solution overnight, and the POC tube was then removed from the metal wire due to slight swelling in ethanol. In Step 2, an air pressure pump was used to infiltrate POMC pre-polymer into the fabricated cladding tube for preparing the fiber core. After thermal crosslinking at 70 °C for 3 days followed by 3 days at 80 °C, the POC cladding/POMC core were seamlessly integrated and a step-index polymer fiber was obtained.

### 2.3. Optical characterization

Refractive indices of POMC and POC were measured with an ellipsometer (J A Woollam M2000-U). Testing samples were prepared by spin-coating 20% (w/v) pre-polymer solutions on cover

slips at a speed of 1000 rpm for 60 s, followed by thermal cross-linking. POC was crosslinked at 70 °C for 7 days and 80 °C for 3 days, while POMC was crosslinked at 70 °C for 3 days, followed by crosslinking at 80 °C for 3 more days. Five samples were tested for each material. For studying light absorption properties, crosslinked POC and POMC cubes were prepared inside cuvettes with a side length of 10 mm. The cuvettes with crosslinked polymers were then placed in a plate reader, and their absorbance at wavelengths ranging from 325 nm to 1000 nm were determined, empty cuvettes were scanned as the background.

### 2.4. Mechanical characterization

Mechanical tests were conducted according to the ASTM D412a standard on an Instron 5966 machine equipped with a 500 N load cell. Tests were performed on polymer films (3 cm in length, and 0.5 cm in width) and fibers (3 cm in length) samples. Each sample was pulled until failure at a rate of 100 mm/min to obtain the stress–strain curve. The initial slope (0–10%) of the curve was used to determine the initial modulus of the sample.

### 2.5. Fiber transmission characterization

A He-Ne laser at a wavelength of 633 nm was used as the light source. The sample fiber was mounted on a V-groove and locked by using plasticine. A 88.3-mm focal length lens was chosen to couple light into the fiber to match the numerical aperture. At the output end, a 10 $\times$  objective was used to collimate the output light from the fiber. The transmission efficiency was calculated based on the laser power before and after the laser enters the fiber with the loss from the optics removed.

### 2.6. Deep tissue fluorescence detection

A 16-week-old Sprague Dawley (SD) rat was euthanized with carbon dioxide (CO<sub>2</sub>) for *in vivo* experiment. A 20 mW 532 nm laser light was used in the optical setup for a deep tissue fluorescence detection study. The Rhodamine B agar gel was placed deep inside the belly area of the SD rat to serve as the fluorescence source. Two citrate-based fibers were inserted into the rat's belly, positioned toward the agar gel, and used respectively for light delivery and collection: Fiber A delivering excitation light from the light source to the Rhodamine B gel, and fiber B collecting the fluorescence emission signal from the gel. At the end of the fiber B, a digital camera was placed to capture fluorescence images, and an Ocean Optics Flame-S spectrometer was used to measure the fluorescence spectrum.

### 2.7. Image transmission through the citrate-based polymeric fiber

To perform image transmission using the citrate-based fiber, calibration of the system response is needed. Individual pixels were projected at the proximal end of the fiber and the corresponding output patterns at the distal end were captured, yielding the intensity impulse response matrix  $H = [h_1, h_2, \dots, h_N]$  of the system, where the  $i^{\text{th}}$  column vector ( $h_i$ ) of  $H$  represents the corresponding output pattern, or the impulse response, of the  $i^{\text{th}}$  input pixel. For a given input image  $\vec{x}$ , its output pattern is given by  $\vec{m} = H\vec{x} + \vec{n}$ , where  $\vec{m}$  is the measured pattern and  $\vec{n}$  is the coherent noise (speckle) due to interference among the output fields produced by different pixels of the input. This equation can be approximately inverted using the least square method  $\vec{x} \approx (H^T H)^{-1} H^T \vec{m}$ . Experimentally, each input pixel (hereafter called super pixel) was comprised of 100 physical pixels (10  $\times$  10) of the DMD. Since the DMD had a pixel size of 13.68  $\mu\text{m}$ , the actual super pixel size at the

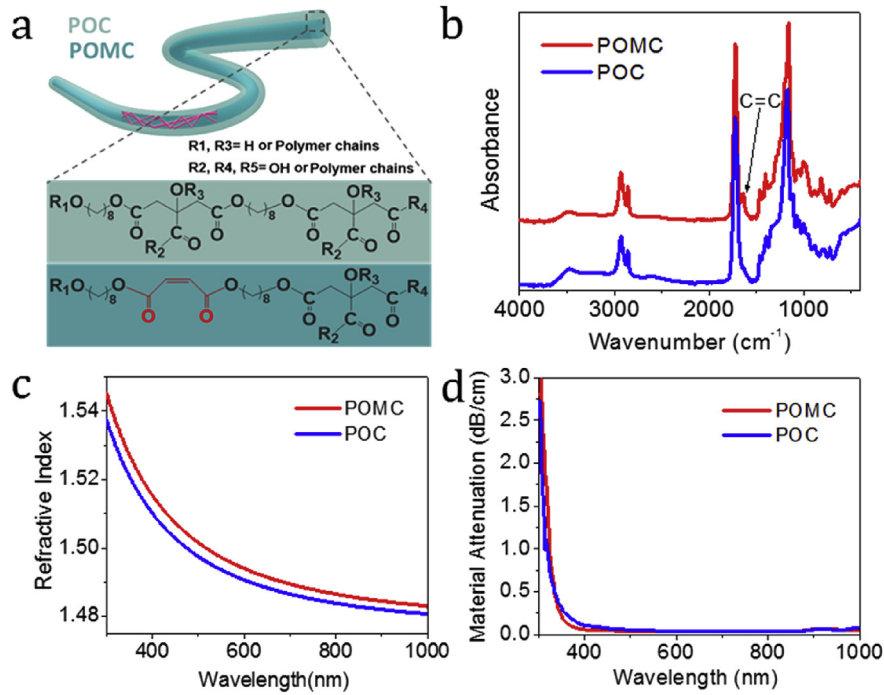


**Fig. 1.** a) Schematic of a flexible core/cladding step-index optical fiber and the chemical structures of the core (POMC) and cladding (POC) materials. b) FTIR spectra of POMC and POC. c) Refractive indices and d) material attenuations of POMC and POC.

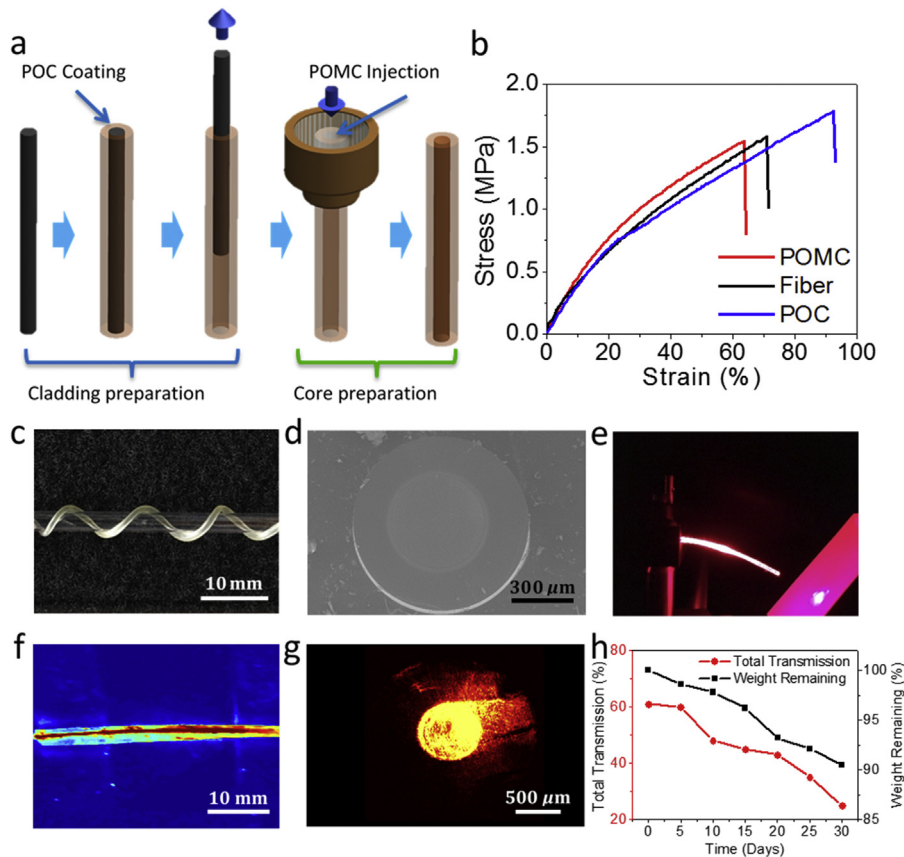


**Fig. 2.** a) Schematic illustration of the fabrication process of the citrate-based polymeric step-index optical fiber. b) Tensile stress-strain curves of crosslinked POMC film, citrate-based optical fiber and crosslinked POC film. c) A photograph of a citrate-based optical fiber twisted around a glass tube, d) Scanning electron microscopy of a cleaved citrate-based optical fiber facet. e) A photograph showing light guidance, f) side view image of light delivery using a citrate-based optical fiber, g) output pattern of a citrate-based optical fiber coupled with a 633 nm He-Ne laser light, and h) Light transmission changes with citrate-based optical fiber degradation.

fiber end after the telescope system was approximately  $9 \times 9 \mu\text{m}^2$ . A total of 64 super pixels ( $8 \times 8$ ) were used during the experiment to generate input images. Output images at the distal end were recorded by a charge-coupled device camera (480 by 720 pixels), with only the core area of the fiber retained in all recorded images. The impulse response  $M$  of the system was a 90000 by 64 matrix, where 90000 is the number of pixels in an output pattern and 64 is the number of available super pixels at the input end. Once the impulse response matrix was measured, a projected input can be reconstructed from its output image.

### 3. Results and discussion

#### 3.1. Synthesis and characterization of POC and POMC

To develop a low-loss step-index bio-optical fiber, the core material requires a higher refractive index than the cladding and yet their mechanical properties (e.g., tensile strength and modulus) should be matched, both of which can be accomplished by tailoring the chemistry of citrate-based polymers. Specifically, we prepared two exemplary citrate-based elastomers, namely, poly(octamethylene citrate) (POC) [13] and poly(octamethylene maleate citrate) (POMC) [11] with nearly identical polymer backbones but slightly different chemical structures (Fig. 1a), arising from the presence of extra maleate groups in POMC by replacing part of citric acid with maleic anhydride during the synthesis process. The structural difference between these two polymers is supported by the appearance of a C=C stretch peak at  $1643 \text{ cm}^{-1}$  in the attenuated total reflectance Fourier transform infrared (ATR-FTIR) spectrum of POMC (Fig. 1b). Although there is only minor difference in the chemical structure between POC and POMC, POMC possesses a higher refractive index than POC over a broad range of wavelength from 300 nm to 1000 nm (Fig. 1c), with an index difference of  $\sim 0.003$ , similar to that between the cladding and the core of conventional silica optical fibers, and corresponding to a fiber numerical aperture of approximately 0.1, which is suitable for a variety of light delivery and collection applications. Material attenuation presented in Fig. 1d indicates that both POC and POMC have relatively low absorption ( $< 0.13 \text{ dB/cm}$ ) at visible and near-infrared wavelengths, which can enable organ scale light delivery and collection.

In addition, POC and POMC films present very soft and flexible mechanical properties in tensile testing, indicated by their initial modulus of  $3.79 \pm 0.45$  and  $4.35 \pm 0.51 \text{ MPa}$ , tensile strengths of  $1.54 \pm 0.16$  and  $1.78 \pm 0.20 \text{ MPa}$ , and elongations of  $62.5 \pm 5.3\%$  and  $92.5 \pm 10.2\%$ . Although POMC shows slightly stronger mechanical properties than POC, their stress-strain curves exhibit matched elastomeric nature when the external strain is less than 20% (Fig. 2b).

In an accelerated degradation study, POC degraded slightly faster than POMC in 0.05 M NaOH solution (Fig. S1a). Under this condition, POC completely degraded in 12 h, while POMC took 16 h to finish the process. The degradation profiles of POC and POMC in phosphate-buffered saline (PBS, pH 7.4) are presented in Fig. S1b. During the first 4 weeks, POC and POMC had matched degradation profiles. Afterwards, POC showed only slightly faster degradation rate than POMC; but there were no significant differences between these two materials even after 12 weeks.

*In vitro* cyto-compatibility of POC and POMC degradation products and films were also tested on 3T3 fibroblast cells using U.S. Food and Drug Administration (FDA)-approved poly(lactic-co-glycolic acid) (PLGA5050) as a control. The polymer degradation products at different dilutions and their films demonstrated minimal cyto-toxicity, and showed no significant difference with the control PLGA5050 (Figs. S2 and S3). POC and POMC polymer films

have also been proved to effectively support cell proliferation, as CCK-8 results indicate 3T3 cells cultured on these films for 7 days have similar growth trend as that on PLGA5050 films. (Fig. S4). In addition, POC and POMC films demonstrate similar *in vivo* foreign body responses as PLLA film after the subcutaneous implantation study with SD rats. As shown in Figs. S5 and S6, 1 week post-implantation, a slight acute inflammatory response was observed and supported by the prominent cell infiltration (H & E staining) including the CD11b positive cells (CD11b staining) in surrounding tissues of each polymer film. After 8 weeks, the cell population around implants declined and thin fibrous capsules between the films and muscle layers were observed suggesting a mild chronic inflammatory reaction triggered by the implanted films, which confirms the good biocompatibility of POC and POMC films and their degradation products.

Due to the above-mentioned material characteristics, flexible biodegradable step-index optical fibers may be developed by using POMC as the core material and POC as the cladding material (Fig. 1a).

#### 3.2. Characterization of polymer step-index fiber

The fabricated polymer fiber is mechanically flexible. The fiber can be easily twisted around a glass tube as shown in Fig. 2c. Their favorable elastomeric properties are supported by the classical stress-strain characteristics of elastomeric materials with an initial modulus of  $3.39 \pm 0.31 \text{ MPa}$ , a tensile strength of  $1.31 \pm 0.25 \text{ MPa}$ , and an elongation of  $61.49 \pm 5.81\%$ , which are consistent with the mechanical properties of individual POC and POMC polymer films (Fig. 2b). Therefore, the soft and flexible mechanical property of the optical fiber alleviates the risk of damaging surrounding tissues and the fiber itself due to body movements, which is a major challenge with traditional brittle silica glass-based optical fibers, making it much safer for *in vivo* biomedical applications. Fibers can be cleaved using normal razor blades; the resultant cross section captured by scanning electron microscopy (SEM) in Fig. 2d shows a smooth facet amicable for optical coupling. Further improvement of facet smoothness can be potentially achieved through ultrafast laser cutting, which may decrease fiber coupling loss and enhance application performance. Based on the SEM results, the thickness of the cladding layer of our fiber can vary from  $150 \mu\text{m}$  to  $1.25 \text{ mm}$ , sufficient to confine light inside the core. Theoretical modeling indicates that, the thickness of the cladding needs to be thicker than  $10 \mu\text{m}$  to effectively minimize power dissipation into the surrounding environment.

In order to examine the optical performance of the fiber, we coupled a 633 nm He-Ne laser light into the citrate-based fiber to test the wave guiding effect. Fig. 2e shows successful light delivery, demonstrating efficient light guiding property of the fiber. The total transmission of the fiber was measured not only at dry condition, but also at wet condition that the fiber may experience *in vivo*. Under both conditions, the tested 3-cm-long fiber was able to yield a  $\sim 58\%$  light transmission. The side view of the fiber with the laser light on is shown in Fig. 2f; the output pattern of the polymer fiber is shown in Fig. 2g. Both figures clearly suggest that the laser light was confined inside the core region. During the measurement, the fiber was physically surrounded by plasticine. Yet, light transmission was not affected in spite of the contact between the fiber and the plasticine, supporting the concept that a step index fiber may achieve efficient light transmission in the fiber core due to the intrinsic cladding layer that shields the optical field from the surrounding tissues when used for *in vivo* applications. The propagation loss of the fiber was determined using the cut-back method. During the measurement, we used a He-Ne laser at a wavelength of 633 nm to measure the fiber loss. In total, we measured three 4-cm-

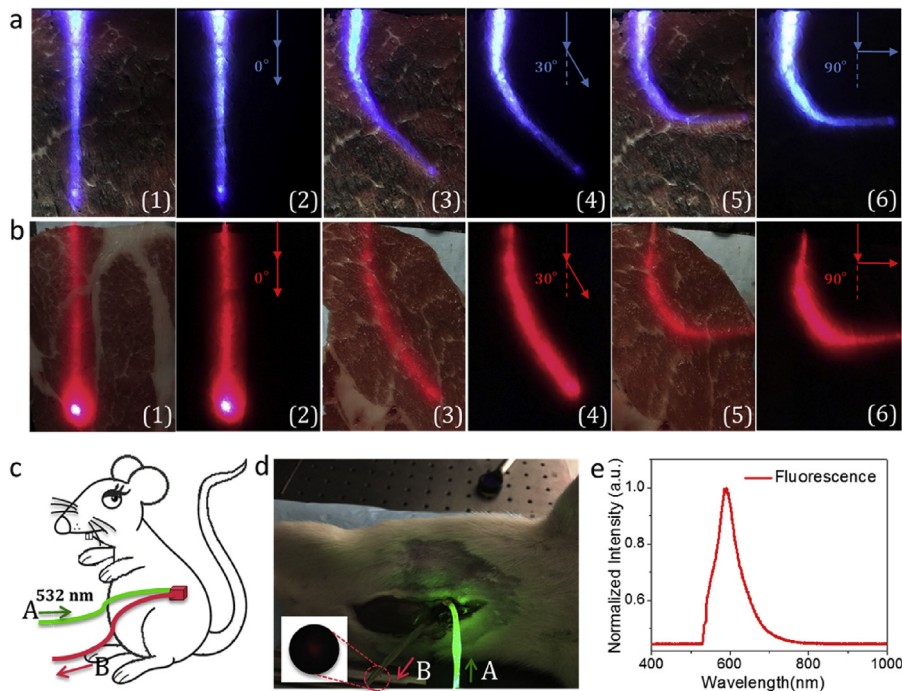


**Fig. 3.** a) Blue light (473 nm) guidance through a citrate-based optical fiber under a thin porcine tissue slice at bending angles of (1, 2) 0°, (3, 4) 30° and (5, 6) 90° recorded with environmental light on (1, 3, 5) and off (2, 4, 6), respectively. b) Red light (633 nm) delivery through a citrate-based optical fiber under a thin porcine tissue slice at bending angles of (1, 2) 0°, (3, 4) 30° and (5, 6) 90° recorded with environmental light on (1, 3, 5) and off (2, 4, 6), respectively. c) Schematic of *in vivo* deep tissue fluorescence detecting with citrate-based optical fibers. d) A photograph of the experiment procedure for *in vivo* deep tissue fluorescence detection with citrate-based optical fibers. e) The fluorescence spectrum collected from the end of the light collection fiber B. (For interpretation of the references to colour in this figure legend, the reader is referred to the web version of this article.)

long fibers. Each cut was performed by using a razor blade and the cut-off length was measured by using a caliper. An average propagation loss of 0.4 db/cm was determined. The additional loss compared with the intrinsic material absorption is likely introduced by the surface roughness of the metal wire mold and fabrication defects. The  $1/e$  penetration depth of our fiber is over 10 cm, thus suitable for *in vivo* experiments.

We also performed *in vitro* degradation studies on the fibers in PBS, which showed that the fibers gradually degraded and reached a weight loss of 9.5% after one month (Fig. 2h). During the period, optical transmissions were also monitored. The results in Fig. 2h indicate that light transmission was reduced from 60% to 25% after degradation for one month. The decrease of light transmission might be resulted from the defects formed at the core/cladding interface during degradation.

### 3.3. Deep tissue light delivery and fluorescence sensing using the citrate based optical fiber

The unique optical and mechanical characteristics coupled with programmable degradation capability of our fibers lend themselves to both *in vitro* and *in vivo* bio-sensing and imaging applications. To confirm the feasibility for light delivery in tissues, a fiber was placed under a piece of thin porcine tissue slice with a thickness of ~2 mm for study (Fig. 3a–b). In Fig. 3a, a 473 nm diode-pumped solid-state laser was coupled into the fiber, and the blue light transmits efficiently along the fiber under different bending angles of 0°, 30° and 90°, which can be verified by the observation of a bright spot at the distal end of the fiber. These results indicate that successful light delivery is possible even at relatively large bending angles. The testing based on a 633 nm He-Ne laser was also conducted on the fiber as shown in Fig. 3b. The fiber shows good light guiding effects for the red light as well. Optical microscopy based

imaging methods such as fluorescence microscopy operating in the visible (Vis) and near-infrared (NIR) regions (400–900 nm) always suffer from limited penetration depth (less than 1 cm) due to light scattering. However, light can be delivered much deeper for *in vivo* imaging and sensing with our citrate-based optical fiber. To further investigate the feasibility of using citrate-based fibers for *in vivo* deep tissue detection and bio-sensing, we performed fluorescence excitation and detection experiments with an animal study on a SD rat and tested our fiber's capability to collect signals from deep tissues. The experimental procedures are depicted in Fig. 3c. An agar gel doped with Rhodamine B was placed deep into the belly area of the rat, and two fibers with a length of 7 cm for excitation light delivery and fluorescence collection were then inserted. As shown by Fig. 3d, the excitation laser light at a wavelength of 532 nm was delivered by the delivery fiber A to illuminate the Rhodamine B-doped agar gel. The emitted red fluorescent light was then detected at the output end of the collection fiber B; a long-pass filter (Chroma ET542lp) was used to block the scattered excitation light (Fig. 3d). The fluorescence spectrum (Fig. 3e) captured by using an optical spectrometer (Ocean Optics Flame) accurately matched with the fluorescence spectrum of the original Rhodamine B gel. The *in vivo* study confirmed an efficient organ scale detection capability of the citrate-based polymeric optical fibers, and demonstrated its mechanical flexibility to be implanted inside body.

### 3.4. Image transmission through citrate based fibers

In recent years, multi-mode fibers have drawn extensive interest for delivery of ultra short laser pulses [35] and endoscopic imaging [1,36–39]. Here we show the proof of concept of using the citrate-based fiber for image transmission, which indicates the tantalizing potential for implantation inside tissues for an extended

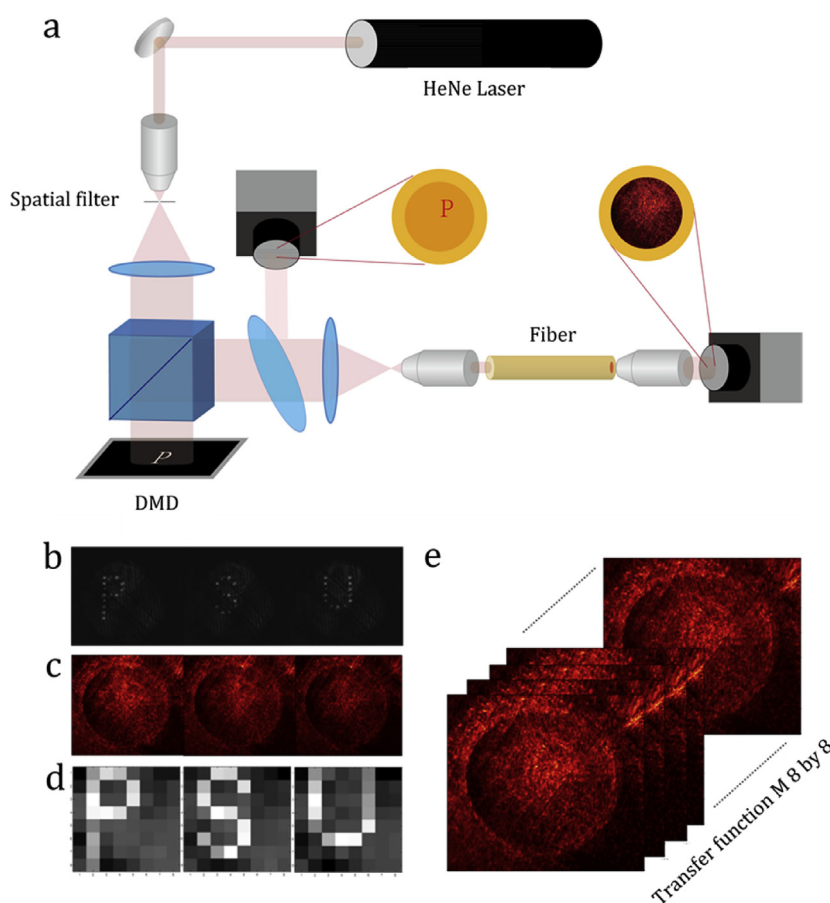


**Fig. 4.** a) Schematic diagram of the experiment setup of the citrate-based optical fiber imaging. b) The projected letter at the citrate-based optical fiber's proximal end, c) output speckle patterns of each input images and d) reconstructed images. e) Recorded impulse response images of the citrate-based optical fiber.

period of time to allow long-term monitoring and imaging. The schematic diagram of the experimental setup is shown by Fig. 4a. A digital micromirror device (DMD) (Texas instruments Discovery 1100) illuminated by a He-Ne laser beam was used to project spatial patterns onto the proximal end of a fiber through an imaging telescope unit consisting of a lens with a 250 mm focal length and a 10X objective lens. In addition, a pellicle beam splitter with a splitting ratio of 8: 92 (reflection: transmission) in conjunction with an imaging setup was used to monitor the pattern projection at the input end. The corresponding output pattern at the distal end of the fiber was recorded by using a charge-coupled device (CCD) camera. Due to the multi-modal propagation, the output of the fiber contained random speckle patterns, which did not resemble the input image at all. In order to retrieve the images, least square retrieval algorithm and pre-calibrated impulse response of the fiber were used to reconstruct the input spatial pattern (see Method 2.7). The experimental result is shown by Fig. 4b–c. The three letters (P, S, and U), initially projected at the proximal end of the fiber, and the corresponding output random speckle patterns at the distal end were shown. By using the pre-recorded impulse responses, which are shown in the right part of Fig. 4e, we were able to retrieve the input pattern (Fig. 4d), demonstrating the potential capability of the citrate-based polymeric optical fiber to deliver spatial images. We would like to point out that the image transmission is affected by fiber bending and movement, which is a known challenge for all multi-mode fiber based imaging applications. Recalibration of the system response function may be required if the modal fields undergo significant changes. Despite this limitation, it has been

shown that imaging through multi-modal waveguides is an effective method, and that the system can exhibit certain degree of tolerance for bending or movement of the fiber [37,38]. Detailed study of the movement and bending tolerance of the citrate-based fibers will be pursued in future efforts.

In addition to sensing and imaging applications, other types of *in vivo* applications, such as optogenetics and photodynamic therapy, can also benefit from our citrate-based polymeric optical fibers. Furthermore, benefited from the favorable biological properties (nontoxic and biodegradable), the citrate-based fiber could be left inside body without the need of a secondary surgery to remove it. This not only reduces cost and pain for patients, but may also improve treatment efficacy, as studies have shown that continuous treatment is more effective over single-time treatment [40]. It is noteworthy that the reactive side groups in citrate-based polymers may be utilized to conjugate functional chemicals, drugs, or biological molecules, and hence fibers with special functionalities, including sensing and potentially disease treatment such as drug delivery, could be designed in the future.

#### 4. Conclusion

Biocompatible and biodegradable optical waveguides are among the most promising and effective tools for overcoming tissue turbidity to enable a plethora of light-based sensing and activation applications in biology and medicine. The present work demonstrates the first citrate-based biodegradable polymeric step index fiber. The use of the citrate platform polymers enables ultra-

fine tuning of refractive index difference between the core and the cladding layers while maintaining identical mechanical characteristics and homogenous biodegradation rate to yield high device integrity. A 0.4 dB/cm loss allows us to perform both *in vitro* and *in vivo* studies inside deep tissue, which show efficient light transmission and optical signal detection abilities. Image transmission through the fiber also shows the feasibility for future deep tissue implantation and *in vivo* imaging. With our method, the refractive indices and mechanical properties of core and cladding materials can be further tailored by modifying chemical structures of the citrate-based platform polymers, which allows control of the number of modes as well as modal properties and seamless integration of the core and the cladding. It is our belief that the citrate-based biodegradable step-index optical fibers may become enabling tools for diverse applications where light delivery, imaging, and/or sensing are desired such as drug delivery, optogenetics, photodynamic therapy, tissue/scaffold imaging and monitoring and so on.

### Acknowledgements

The authors would like to acknowledge financial support from the National Institutes of Health (NCI CA182670 and NHLBI HL118498). The authors also thank Dr. Jinshan Guo and Gerald L. Kirk for editing assistance.

### Appendix A. Supplementary data

Supplementary data related to this article can be found at <http://dx.doi.org/10.1016/j.biomaterials.2017.08.003>.

### References

- [1] I.N. Papadopoulos, S. Farahi, C. Moser, D. Psaltis, High-resolution, lensless endoscope based on digital scanning through a multimode optical fiber, *Biomater. Opt. Express* 4 (2013) 260–270.
- [2] L. Tong, R.R. Gattass, J.B. Ashcom, S. He, J. Lou, M. Shen, I. Maxwell, E. Mazur, Subwavelength-diameter silica wires for low-loss optical wave guiding, *Nature* 426 (2003) 816–819.
- [3] M. Choi, J.W. Choi, S. Kim, S. Nizamoglu, S.K. Hahn, S.H. Yun, Light-guiding hydrogels for cell-based sensing and optogenetic synthesis *in vivo*, *Nat. Photonics* 7 (2013) 987–994.
- [4] S.T. Parker, P. Domachuk, J. Amsden, J. Bressner, J.A. Lewis, D.L. Kaplan, F.G. Omenetto, Biocompatible silk printed optical waveguides, *Adv. Mater* 21 (2009) 2411–2415.
- [5] A. Jain, A.H.J. Yang, D. Erickson, Gel-based optical waveguides with live cell encapsulation and integrated microfluidics, *Opt. Lett.* 37 (2012) 1472–1474.
- [6] S. Nizamoglu, M.C. Gather, M. Humar, M. Choi, S. Kim, K.S. Kim, S.K. Hahn, G. Scarcelli, M. Randolph, R.W. Redmond, Bioabsorbable polymer optical waveguides for deep-tissue photomedicine, *Nat. Commun.* 7 (2016).
- [7] M. Choi, M. Humar, S. Kim, S. Yun, Step-index optical fiber made of biocompatible hydrogels, *Adv. Mater* 27 (2015) 4081–4086.
- [8] J. Guo, X. Liu, N. Jiang, A.K. Yetisen, H. Yuk, C. Yang, A. Khademhosseini, X. Zhao, S. Yun, Highly stretchable, strain sensing hydrogel optical fibers, *Adv. Mater* 28 (2016) 10244–10249.
- [9] M.B. Applegate, G. Perotto, D.L. Kaplan, F.G. Omenetto, Biocompatible silk step-index optical waveguides, *Biomater. Opt. Express* 6 (2015) 4221–4227.
- [10] J. Guo, W. Wang, J. Hu, D. Xie, E. Gerhard, M. Nistic, D. Shan, G. Qian, S. Zheng, J. Yang, Synthesis and characterization of anti-bacterial and anti-fungal citrate-based mussel-inspired bioadhesives, *Biomaterials* 85 (2016) 204–217.
- [11] D. Gyawali, R.T. Tran, K.J. Guleserian, L. Tang, J. Yang, Citric-acid-derived photo-cross-linked biodegradable elastomers, *J. Biomater. Sci. Polym. Ed.* 21 (2010) 1761–1782.
- [12] J. Yang, Y. Zhang, S. Gautam, L. Liu, J. Dey, W. Chen, R.P. Mason, C.A. Serrano, K.A. Schug, L. Tang, Development of aliphatic biodegradable photoluminescent polymers, *Proc. Natl. Acad. Sci.* 106 (2009) 10086–10091.
- [13] J. Yang, A.R. Webb, G.A. Ameer, Novel citric acid-based biodegradable elastomers for tissue engineering, *Adv. Mater* 16 (2004) 511–516.
- [14] R.T. Tran, J. Yang, G.A. Ameer, Citrate-based biomaterials and their applications in regenerative engineering, *Annu. Rev. Mater. Res.* 45 (2015) 277–310.
- [15] J. Guo, Z. Xie, R.T. Tran, D. Xie, D. Jin, X. Bai, J. Yang, Click chemistry plays a dual role in biodegradable polymer design, *Adv. Mater* 26 (2014) 1906–1911.
- [16] R.T. Tran, W.M. Choy, H. Cao, I. Qattan, J. Chiao, W.Y. Ip, K.W.K. Yeung, J. Yang, Fabrication and characterization of biomimetic multichanneled crosslinked-urethane-doped polyester tissue engineered nerve guides, *J. Biomed. Mater. Res. Part A* 102 (2014) 2793–2804.
- [17] L.-C. Su, H. Xu, R.T. Tran, Y.-T. Tsai, L. Tang, S. Banerjee, J. Yang, K.T. Nguyen, In situ re-endothelialization via multifunctional nanoscaffolds, *ACS Nano* 8 (2014) 10826–10836.
- [18] D. Sun, Y. Chen, R.T. Tran, S. Xu, D. Xie, C. Jia, Y. Wang, Y. Guo, Z. Zhang, J. Guo, Citric acid-based hydroxyapatite composite scaffolds enhance calvarial regeneration, *Sci. Rep.* 4 (2014) 6912.
- [19] D. Xie, J. Guo, M.R. Mehdizadeh, R.T. Tran, R. Chen, D. Sun, G. Qian, D. Jin, X. Bai, J. Yang, Development of injectable citrate-based bioadhesive bone implants, *J. Mater. Chem. B* 3 (2015) 387–398.
- [20] Y. Guo, R.T. Tran, D. Xie, Y. Wang, D.Y. Nguyen, E. Gerhard, J. Guo, J. Tang, Z. Zhang, X. Bai, Citrate-based biphasic scaffolds for the repair of large segmental bone defects, *J. Biomed. Mater. Res. Part A* 103 (2015) 772–781.
- [21] J. Tang, J. Guo, Z. Li, C. Yang, D. Xie, J. Chen, S. Li, S. Li, G.B. Kim, X. Bai, A fast degradable citrate-based bone scaffold promotes spinal fusion, *J. Mater. Chem. B* 3 (2015) 5569–5576.
- [22] Z. Xie, C.B. Paras, H. Weng, P. Punnakitikashem, L.-C. Su, K. Vu, L. Tang, J. Yang, K.T. Nguyen, Dual growth factor releasing multi-functional nanofibers for wound healing, *Acta Biomater.* 9 (2013) 9351–9359.
- [23] M. Mehdizadeh, H. Weng, D. Gyawali, L. Tang, J. Yang, Injectable citrate-based mussel-inspired tissue bioadhesives with high wet strength for sutureless wound closure, *Biomaterials* 33 (2012) 7972–7983.
- [24] J. Guo, G.B. Kim, D. Shan, J.P. Kim, J. Hu, W. Wang, F.G. Hamad, G. Qian, E.B. Rizk, J. Yang, Click chemistry improved wet adhesion strength of mussel-inspired citrate-based antimicrobial bioadhesives, *Biomaterials* 112 (2017) 275–286.
- [25] Z. Xie, N. V. Aphale, T.D. Kadapure, A.S. Wadajkar, S. Orr, D. Gyawali, G. Qian, K.T. Nguyen, J. Yang, Design of antimicrobial peptides conjugated biodegradable citric acid derived hydrogels for wound healing, *J. Biomed. Mater. Res. Part A* 103 (2015) 3907–3918.
- [26] J. Yang, A.R. Webb, S.J. Pickerill, G. Hageman, G.A. Ameer, Synthesis and evaluation of poly (diol citrate) biodegradable elastomers, *Biomaterials* 27 (2006) 1889–1898.
- [27] A.S. Wadajkar, T. Kadapure, Y. Zhang, W. Cui, K.T. Nguyen, J. Yang, Dual-imaging enabled cancer-targeting nanoparticles, *Adv. Healthc. Mater* 1 (2012) 450–456.
- [28] Z. Xie, Y. Zhang, L. Liu, H. Weng, R.P. Mason, L. Tang, K.T. Nguyen, J. Hsieh, J. Yang, Development of intrinsically photoluminescent and photostable polylactones, *Adv. Mater* 26 (2014) 4491–4496.
- [29] Y. Zhang, R.T. Tran, I.S. Qattan, Y.-T. Tsai, L. Tang, C. Liu, J. Yang, Fluorescence imaging enabled urethane-doped citrate-based biodegradable elastomers, *Biomaterials* 34 (2013) 4048–4056.
- [30] D. Gyawali, S. Zhou, R.T. Tran, Y. Zhang, C. Liu, X. Bai, J. Yang, Fluorescence imaging enabled biodegradable photostable polymeric micelles, *Adv. Healthc. Mater* 3 (2014) 182–186.
- [31] J. Li, Y. Tian, D. Shan, A. Gong, L. Zeng, W. Ren, L. Xiang, E. Gerhard, J. Zhao, J. Yang, Neuropeptide YY 1 receptor-mediated biodegradable photoluminescent nanobubbles as ultrasound contrast agents for targeted breast cancer imaging, *Biomaterials* 116 (2017) 106–117.
- [32] Z. Xie, Y. Su, G.B. Kim, E. Selvi, C. Ma, V. Aragon-Sanabria, J. Hsieh, C. Dong, J. Yang, Immune cell-mediated biodegradable theranostic nanoparticles for melanoma targeting and drug delivery, *Small* 13 (2017).
- [33] J. Hu, J. Guo, Z. Xie, D. Shan, E. Gerhard, G. Qian, J. Yang, Fluorescence imaging enabled poly (lactide-co-glycolide), *Acta Biomater.* 29 (2016) 307–319.
- [34] J.P. Kim, Z. Xie, M. Creer, Z. Liu, J. Yang, Citrate-based fluorescent materials for low-cost chloride sensing in the diagnosis of cystic fibrosis, *Chem. Sci.* 8 (2017) 550–558.
- [35] E.E. Morales-Delgado, S. Farahi, I.N. Papadopoulos, D. Psaltis, C. Moser, Delivery of focused short pulses through a multimode fiber, *Opt. Express* 23 (2015) 9109–9120.
- [36] M. Plöschner, T. Tyc, T. Čizmar, Seeing through chaos in multimode fibres, *Nat. Photonics* 9 (2015) 529–535.
- [37] T. Čizmar, K. Dholakia, Exploiting multimode waveguides for pure fibre-based imaging, *Nat. Commun.* 3 (2012) 1027.
- [38] Y. Choi, C. Yoon, M. Kim, T.D. Yang, C. Fang-Yen, R.R. Dasari, K.J. Lee, W. Choi, Scanner-free and wide-field endoscopic imaging by using a single multimode optical fiber, *Phys. Rev. Lett.* 109 (2012) 203901.
- [39] R. Barankov, J. Mertz, High-throughput imaging of self-luminous objects through a single optical fibre, *Nat. Commun.* 5 (2014).
- [40] M.H. Roozeboom, M.A. Aardoom, P.J. Nelemans, M.R.T.M. Thissen, N.W.J. Kelleners-Smeets, D.I.M. Kuijpers, K. Mosterd, Fractionated 5-aminolevulinic acid photodynamic therapy after partial debulking versus surgical excision for nodular basal cell carcinoma: a randomized controlled trial with at least 5-year follow-up, *J. Am. Acad. Dermatol.* 69 (2013) 280–287.